BERKELEY LAB

ERNEST ORLANDO LAWRENCE
BERKELEY NATIONAL LABORATORY

Gallium Manganese Phosphide synthesized by Ion Implantation and Pulsed-Laser Melting

REPORT

on research conducted at the

University of California, Berkeley

in the period

September 1, 2009 - January 31, 2010

Author:
Thomas Winkler

Advisors:
Prof. Alberta Bonanni (JKU)
Prof. Oscar Dubon (UCB)

Linz, 2010-04-30

It is good to have an end to journey toward,

but it is the journey that matters in the end.

- Ursula K. LeGuin

Declarations

I hereby declare that I have authored this report independently, that I have not used other than the declared sources or resources, and that I have explicitly marked all material which has been quoted either literally or by content from the used sources.

- Thomas Winkler

I hereby declare that Thomas Winkler completed his objectives for the research stay in Berkeley to my full satisfaction.

- Alberta Bonanni, Assoc. Prof.

Contents

1 Introduction **1**

2 GaMnP Background and Processing **5**

2.1 Theory of GaMnP 5

2.2 Ion Implantation and Pulsed-Laser Melting 9

2.3 Defect Compensation 13

3 Experimental Results **17**

3.1 Hall Effect 17

3.2 Magnetometry 20

3.3 Electric Transport 28

3.4 Structural Analysis 32

4 Conclusions & Outlook **39**

Acknowledgments **I**

Bibliography **III**

1 Introduction

As conventional electronics is fast approaching its limits - *e.g.* that of transistor size and switching speed - viable alternatives need to be explored. One possible direction is *spintronics*, which is based on the control of information not only *via* electronic charge, but also through the intrinsic spin of the carriers, *i.e.* their magnetic moments. So-called dilute magnetic semiconductors (DMSs), especially the ferromagnetic variety, represent a remarkable work-bench for the study and demonstration of spintronic functionalities. In these systems, magnetic impurities are randomly substituted in the host matrix and coupled by indirect exchange mechanisms involving the semiconductor charge carriers.

DMSs are not only a means to an end, but very exciting materials in their own right, exhibiting many striking phenomena whose interpretation and modelling are extremely challenging. Much of the research has focused on III-Mn-V systems [Jun06], where a few percent of group III atoms are replaced by Manganese, which acts as a source of both magnetic moment and carriers that facilitate long-range ordering. Especially GaMnAs has been extensively investigated, mainly due to the fact that it is based on GaAs, *i.e.* one of the most studied and well-understood semiconductors. With some effort, Curie temperatures up to 185 K have been achieved [Nov08] and represent a major progress from the initial III-Mn-V observation of 7.5 K [Ohn92] in InMnAs, but are still very far from the desirable room-temperature ferromagnetism.

Both in the search for higher temperature materials and in an effort to better understand the mechanisms governing the magnetic behavior of III-Mn-V compounds, many other members of this class are currently under investigation. Partly because of the theoretical predictions in [Die00], much of the focus has been on GaMnN. GaMnP, which also has potential for establishing host material trends, has in comparison been greatly neglected, mostly due to the fact that fabrication by traditional methods, *e.g.* Molecular Beam Epitaxy (MBE) or Chemical Vapor Deposition (CVD), is exceedingly difficult. To date, only one group reported epitaxial growth of GaMnP [Ove01], but carrier-mediated ferromagnetism was never clearly established [Sca05]. The novel method of ion-implantation and subsequent laser annealing for GaMnP fabrication first presented in [Sca03] and backed with stringent study of the produced samples - most importantly confirming the DMS character - represented a crucial step toward the understanding of the system, and indeed remarkable has been made since [Sca06].

Among the lines of study pursued was, as with most DMSs, the behavior of the material upon varying the concentration of magnetic impurities [Far06]. In III-Mn-V systems, however, this approach only explores part of the available parameter space, because - as stated before - Manganese contributes magnetic moments and carriers simultaneously. Thus, it is of great interest to decouple these effects and vary solely the carrier concentration. Such control has been demonstrated mainly by co-doping with acceptors or donors, to some extent also in GaMnP [Sca08b]. Co-doping, however, suffers from a number of physical and technical limitations. Thus, a new approach only recently applied to GaMnAs [May10], which utilizes native defects for compensation, has been adapted in this work for the study of GaMnP.

In this report, I first lay out the necessary background information on theory and sample processing in Chapter 1. In Chapter 2, the experiments and their results are presented and interpreted. The major finding is a highly linear correlation between hole concentration and magnetic properties in GaMnP, which is strikingly similar to that observed in the aforementioned GaMnAs study. This is another indication that the mechanisms giving rise to these systems' magnetism are intimately related in spite of their stark electronic differences. Finally, in Chapter 4 I will draw overarching conclusions and discuss relevant future research.

2 GaMnP Background and Processing

2.1 Theory of GaMnP

In GaMnP, a few atomic percent of the Gallium host sublattice are replaced with Manganese (cf. Figure 2.1). The transition metal, with its 5 $3d$-electrons, is an obvious source of localized magnetic moment, and in the zinc-blende semiconductor matrix furthermore acts as an acceptor. Magnetic order in the system is brought about by the thus provided holes, whose spins - through so-called kinetic $p - d$ exchange - couple antiferromagnetically to those of the Mn ions. *Via* interaction of the holes with multiple ions, Manganese spins are aligned in parallel, resulting in ferromagnetism. The extent and stability of the magnetic order - in other words, the Curie temperature T_C - due to the carrier-mediated mechanism depends not only on the substitutional fraction of Manganese, x, but also on the hole concentration p.

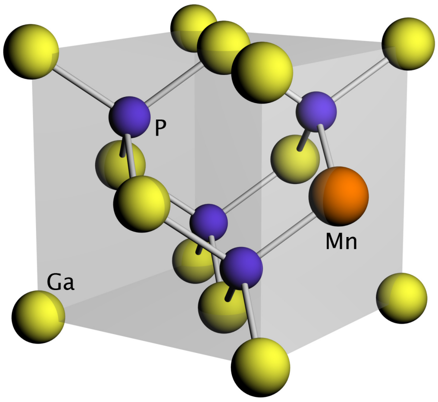

Fig. 2.1: Illustration of GaMnP crystal structure.

In contrast to the III-Mn-V “reference system" GaMnAs, GaMnP exhibits insulating behavior for the whole range of x studied. The host bandgap is nearly twice as large at 2.26 eV [Sik01], and the Manganese acceptor level is almost four times as deep at ~ 400 meV [Cle85]. In effect, the holes are of a much more localized nature. Thus, mean-field models fall short of providing a theoretical basis for the observed ferromagnetism in this system, which has beyond reasonable doubts been established by a combination of magnetometry, magnetotransport and X-ray techniques [Sca05; Sto06] and in the best samples persists up to $T_C \approx 65$ K [Far06].

The theory proposed in [Sca05] and supported by transport measurements, far-IR photoconductivity and THz spectroscopy is that the holes reside in a Manganese impurity band, centered at the acceptor level. The breadth of this band is determined by the doping level, and at least up to the as yet highest concentrations of $x = 0.042$ remains independent from the valence band, as illustrated in Figure 2.2. The resultant gap is what could be investigated with the aforementioned techniques.

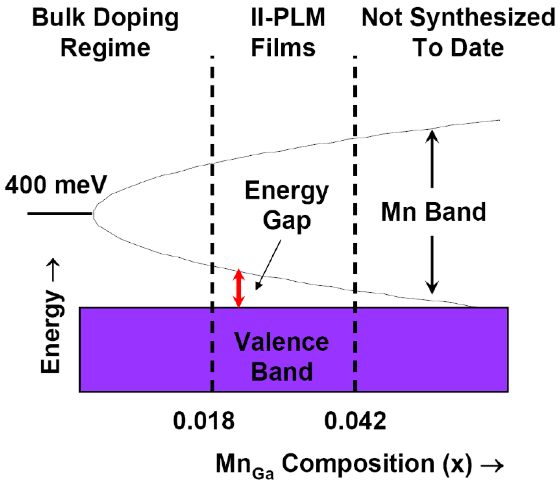
Bulk Doping
Regime
II-PLM
Films
Not Synthesized
To Date
400 meV
Energy
Gap
Mn Band
Energy →
Valence
Band
0.018
0.042
Mn$_{Ga}$ Composition (x) →

Fig. 2.2: Illustration of the impurity band model for GaMnP. [Sca06]

It should not go unmentioned that while the impurity band theory is the only one found in the literature for GaMnP, this is in great part due to its novelty. While theories resting on free valence-band holes clearly fail to describe the behavior of the system, a model based on a merged impurity band with localized holes below the mobility edge [Jun07] could also be applied. Distinguishing between these models, however, is not possible based on the data available to date.

Taking a closer look at the magnetic properties of GaMnP, it becomes apparent that they are not isotropic [Bih07]. As is usual for epitaxially grown films, the compressive strain results in a magnetic global hard axis normal to the surface, *i.e.* along [001]. In the sample plane, two other anisotropy fields can be observed. The stronger leads to a $\langle 110 \rangle$ easy axis, while the weaker, uniaxial one breaks the equivalency and determines the $[1\bar{1}0]$ global easy axis. It has been determined that the anisotropic behavior is in many respects very similar to that in GaMnAs, with control over the magnetic axis through various techniques demonstrated [Sto07; Sto08].

In terms of electrical properties, a simple model routinely used for other doped semiconductors with insulating behavior has been found to reasonably cover GaMnP: $\sigma = \sigma_1 e^{-\frac{\varepsilon_1}{kT}} + \sigma_3 e^{-\frac{\varepsilon_3}{kT}}$ [Shk84; Sca05]. It describes the overall conductivity σ as being based on two different thermally-activated mechanisms with activation energies ε_i. The second term therein describes conduction of carriers by hopping between empty states on adjacent impurity sites. The first term describes conduction due to excitation across the gap between impurity level (or, at high concentrations, band) and conduction/valence band. A middle term usually describing a different hopping mechanism can be omitted for this system. The model has one major shortfall, however, as it was originally only intended for isolated impurities. As such, it fails to take into account certain features of a broadened impurity band, like shifts of the Fermi energy E_F with temperature. It should be noted that if a mobility edge rather than an energy gap represents the barrier in the first term, the model remains unchanged.

One other feature of the material that is of some importance for understanding this work is its anomalous Hall effect. As with all ferromagnetic materials, the Hall resistivity in GaMnP contains a term dependant on magnetization M in addition to the regular, field-dependant contribution: $\rho_{xy} = R_H \cdot B + A \cdot M$. And as in other DMSs like GaMnAs, this AHE is very pronounced, the resistivity clearly following trends in sample magnetization, like the transition from ferromagnetic to paramagnetic at T_C [Sca05]. This makes the information contained in the regular Hall coefficient R_H - *i.e.* carrier concentration - hard to access. There are naturally some regions in the parameter space where the regular term dominates. However, even at room temperature, the anomalous contribution can be significant, as has been predicted and observed in GaMnAs [Ruz04]. And higher temperatures or alternatively fields, while demonstrated to achieve the desired effect [Edm02], are not generally feasible for practical reasons.

2.2 Ion Implantation and Pulsed-Laser Melting

Ion implantation is a rather straightforward process in which the ions to be implanted into a sample are accelerated into it. Besides the type and amount of ions, the depth scale is the most important figure of merit in the process, with a profile generally resembling a Gaussian [Sca06]. Its center - the projected range of the ions - depends on a number of factors including ion species, energy and incidence angle as well as on the target's density and structure. Since the ions are slowed down by inelastic scattering on sample atoms, one ion can displace a significant number of these. When trying to implant GaP with Mn in concentrations relevant for ferromagnetic behavior, this will result in sample amorphization down to a depth that roughly corresponds to the projected range [Pea88], terminating in a highly defective end-of-range layer.

In consequence, some annealing process is needed to restore crystalline order to the sample and to substitutionally incorporate the Mn atoms. Pulsed-laser melting presents itself because it is, like the implantation process and in contrast to other methods, not governed by thermodynamic equilibrium, but rather by kinetics. As the process is implemented here, a spatially homogenized KrF excimer laser ($\lambda = 248$ nm) with pulses of 18 ns FWHM is utilized. Its optical absorption length is less than 10 nm in GaP, while the thermal diffusion length is at least one order of magnitude greater - the latter thus setting the relevant length scale [Sca06]. The process is defined by the rapid heat flow from the thin absorbing layer into the sample, whereby the sample is melted. Resolidification then occurs as liquid-phase epitaxy from the underlying crystal structure at a rate in the $\mathrm{m\,s^{-1}}$range. This results in so-called solute trapping, whereby the implanted Mn are incorporated into the crystal structure, faster than it can diffuse out or phase-separate, and thus in quantities well exceeding equilibrium solubility.

With a given laser and given material, the most important free parameter is the integrated pulse fluence F. It is directly proportional to the thermal diffusion length in the regime of interest, *i.e.* below the point where ablation becomes the dominating effect [Sca06]. Thus a critical fluence F_{XM} can be defined as that fluence where the melt extends all the way to the crystalline layers. If $F < F_{XM}$, defects at the end of range can propagate through the implanted layer, or polycrystalline growth may occur. $F > F_{XM}$ is also not desirable: while film quality remains high for a certain range, Manganese incorporation is adversely affected by the excess energy [Dub06].

It should be noted that despite these fast processes, still not all the implanted Mn is incorporated, but up to 50 % transported to the surface by the resolidification front [Dub06]. The limiting factor is mainly the laser pulse duration - with a picosecond laser, an even higher degree of incorporation would be possible due to the higher resulting quench rates [Sca06]. This also places an upper limit on the ion implantation dose, above which no additional Mn will be incorporated substitutionally. The aggregation of Mn at the surface is accompanied by a breakdown of epitaxy in that region [Sca03], so to assess the magnetic properties of dilute GaMnP, this layer has to be removed, which can be accomplished by extended etching in HCl.

Even in such processed samples the typical substitutional fraction is in the range of 70 % to 80 % [Sca06]. This holds for both GaMnP and GaMnAs and is similar to what is achieved in LT-MBE growth of GaMnAs, thus not a bad sign. What is interesting is that while the remaining Mn in MBE grown samples is generally of interstitial nature, it is not in II-PLM ones [Sca03]. It is thought to instead reside at random positions in the crystal lattice, *i.e.* at such that are neither substitutional nor interstitial, although formation of small clusters of Mn can not be excluded as an explanation either.

Comparison of GaMnAs samples from II-PLM and LT-MBE is also where the validity of the process for fabrication of DMSs is established [Sca08a]. The properties of samples with the same x for the two techniques are identical within the variances within the separate ones. x in the case of II-PLM, as the distribution of Mn is generally not flat, is taken as its maximum, which also goes to show that this layer determines the magnetic properties of the whole sample.

For the experiments discussed here, a commercial (001)-oriented GaP wafer - unintentionally n-type; $n \sim 10^{16} - 10^{17}$ cm^{-3} - was implanted at an energy of 50 keV and an incidence of 7° with $2 \cdot 10^{16}\mathrm{Mn}^{+}\,\mathrm{cm}^{-2}$, close to the appropriate limit as discussed above. After cleaving into eight pieces (#06-13) they were individually irradiated at $F \approx F_{XM} \approx 0.4\ \mathrm{J\,cm}^{-2}$ and subsequently subjected to 24 h HCl etching. These parameters have previously been used to produce samples with $x \approx 0.038$ [Far06].

2.3 Defect Compensation

In GaMnP, as discussed in Section 2.1, Mn provides both the magnetic moments and the holes, and its behavior has already been studied in detail for various x [Far06]. To gain a better understanding of these systems, a decoupling of the two parameters is desirable. Previous attempts with donor co-doping have been made by introducing S or Te in addition to Mn during ion implantation [Sca05; Sca08b]. These studies, while revealing some insight, unfortunately have some limitations and drawbacks. Besides the intended hole compensation, unintentional effects (*i.e.* lattice distortion, S/Te-Mn complex formation, ...) from the dopants which are present in quantities similar to that of Mn can not be excluded. Also, for each level of compensation, a separate sample is needed which makes the process prone to further error, especially in the technically difficult case of Te.

Therefore, compensation of holes by introduction of native defects was applied in this study. Point defects have some time ago been shown to act as dopants of amphoteric nature [Wal89]. The deciding factor is the location of the Fermi energy in relation to the material-dependent Fermi stabilization energy [Wal88]. In GaMnP as in GaMnAs, E_{FS} is approximately centered in the energy gap, while E_F is significantly closer to the valence band, thus native defects act predominately as donors - just what is needed for this study.

The advantages of this method are numerous. Point defects can be introduced in almost arbitrary abundance simply by high energy ion irradiation. As a single ion can produce orders of magnitude more defects, the influence of the ion species itself can be judged to be negligible. Moreover, the damage is cumulative, thus allowing the study of multiple levels of compensation with a single sample, very much simplifying the process from a technical perspective. Last but not least, the dispersion of the defects throughout the crystal can be considered to be truly random, as they will not form bonds with the atomic species and thus not suffer from potential clustering.

The approach is not entirely novel for study of a III-Mn-V system, as it has already been applied to GaMnAs [May10]. That work, however, serves to both establish the validity of this technique and to provide a basis for comparisons between material systems.

To select appropriate parameters, simulations were run with the SRIM (stopping range of ions in matter) software [Zie08]. Based on these - purely kinetic - Monte Carlo simulations, it was determined that Argon ions at an energy of 33 keV and an incidence of 7° would most likely yield a vacancy depth profile in reasonable agreement with Mn distributions in typical GaMnP samples [Sca06] as determined by secondary ion mass spectrometry (SIMS), Figure 2.3. The simulations suggest 499 vacancies being formed per ion, with the peak in vacancy concentration occurring at a depth of 20 nm.

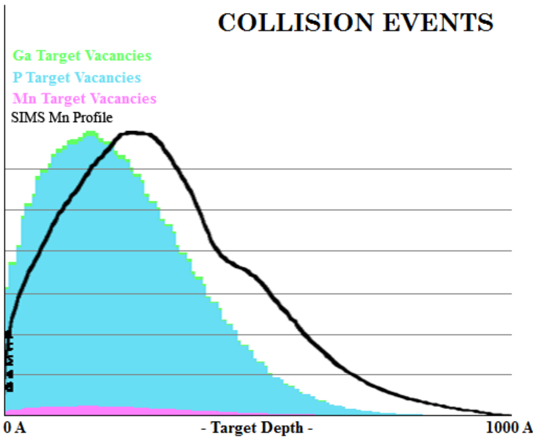

Fig. 2.3: Simulated vacancies under Argon irradiation with the parameters described, overlaid with a typical [Sca06] Manganese depth profile as determined by SIMS. Units are arbitrary.

The dose per irradiation was first chosen at $7 \cdot 10^{10}$ $\mathrm{Ar}^{+}\,\mathrm{cm}^{-2}$, then increased according to the observed effects, with the tenth irradiation ($1 \cdot 10^{12}$ $\mathrm{Ar}^{+}\,\mathrm{cm}^{-2}$) bringing the final integrated dose to $5.77 \cdot 10^{12}$ $\mathrm{Ar}^{+}\,\mathrm{cm}^{-2}$.

3 Experimental Results

3.1 Hall Effect

The anomalous Hall effect in GaMnP, as laid out in Section 2.1, precludes keeping track of the carrier concentration by this usually direct and simple method. Applying electrochemical capacitance voltage (ECV) profiling, while successfully demonstrated for as-grown GaMnAs [Yu02], is also not an option - tracking for defect compensated samples has been found to be unreliable [May10]. The highly insulating properties of GaMnP also make accurate measurements even on the uncompensated samples difficult.

Thus, a GaP:Zn control sample (#05) was processed in parallel to the GaMnP ones (cf. Section 2.2). In this more traditional (non-ferromagnetic) semiconductor system, tracking carrier concentration by means of Hall effect presents no problem. The carrier removal rate with Ar^+ irradiation can reasonably be assumed to be the same in both systems, as has also been done in similar experiments [May10]. In consequence, by conducting

Hall effect measurements on the control sample after each processing step, the Ar^+ doses could be related to the number of holes removed.

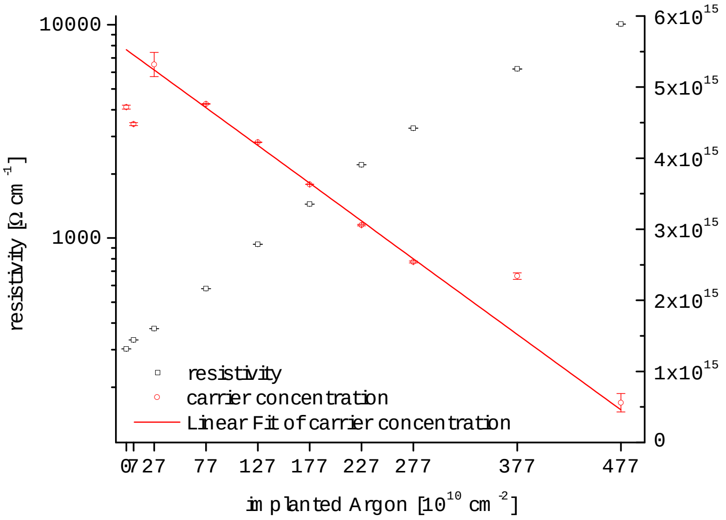

Fig. 3.1: Sheet resistance (black, left scale) and carrier concentration (red, right scale) of GaP:Zn control sample as determined by Hall effect measurements. Line is best linear fit through points 3 to 8 and 10.

The measurements were done with four pressed-on Indium contacts, which were determined to be Ohmic at all temperatures by I-V curves, in Van der Pauw geometry at a temperature of 290 K, at magnetic fields between 0.5 T and 5 T. The results in Figure 3.1, as expected, show a linear behavior of the carrier concentration in relation to the implanted Ar^+. Three deviations from this can be observed and have been attributed to contact problems - contacts had to be replaced after the second, eighth and ninth measurements. It should be noted that the absolute carrier concentration can thus not be relied on, but is by design only of secondary interest. A linear fit disregarding these points yields a carrier removal rate of -1100 ± 110 holes per Argon ion. From this section forward, x-axes will oftentimes display relative hole concentration Δp - rather than implanted Ar^+ dose - which is the difference of hole concentration to an uncompensated sample based on the hole removal per Ar^+ derived here.

Considering the simulated ≈ 500 vacancies per implanted Ar^+ (cf. Section 2.3), an effective compensation of 2.2 ± 0.2 holes per vacancy can be calculated. This value can be compared to the 0.91 holes per vacancy observed in GaAs-based systems [May10]. The difference is assumed to be due to the different location of E_{FS} compared to both the Mn acceptor level and the valence band, and thus to the initial E_F.

While, as discussed above, an absolute value for the hole concentration for GaMnP could not accurately be determined, one can deduce upper and lower bounds for it. From the structural analysis in Section 3.4, an upper limit of $\approx 7.5 \cdot 10^{15}$ cm^{-2} and a lower limit of $\approx 4.5 \cdot 10^{15}$ cm^{-2} can be inferred. Also, the trends from Section 3.2 and Section 3.3 suggest that not significantly more than 100 % of the initial holes had been compensated after the last ion irradiation. Thus, the ultimate removal of $\approx -6.5 \cdot 10^{15}$ cm^{-2} holes represents control of the hole concentration over a very wide range.

3.2 Magnetometry

Seeing as magnetism is the defining characteristic of a DMS system, a variety of magnetic measurements was performed on the samples. For these, a Quantum Design magnetic property measurement system (MPMS) superconducting quantum interference device (SQUID) magnetometer was employed. The main categories of data gathered were of magnetic moment m i) for variable magnetizing fields H up to ±50000 Oe at a temperature $T = 5$ K and ii) for variable T between 5 K and 65 K at $H = 10$ Oe, in both cases employing zero-field cooling.

From the m vs. H datasets, scanned from the lowest to the highest field as in Figure 3.2a, first the dominant diamagnetic background was determined for each measurement. Sources of the diamagnetic signal include the GaP substrate, the sample holder and most kinds of potential contamination. This was accomplished by producing separate linear fits to the data in the ranges below -5000 Oe and above 5000 Oe. Based on the averaged slope k_{dia}, $k_{dia} \cdot H$ was subsequently subtracted from all data of that measurement. While, due to the low magnetizing field used, almost unnoticeable in m vs. T data, only this treatment revealed the magnetic response of GaMnP as seen in Figure 3.2b. This also allows for a meaningful expression of m in terms of Bohr magnetons μ_B per substitutional Manganese $\mathrm{Mn_{Ga}}$, and thus for better comparison with other works. While possibly not entirely sound as laid out in Section 3.4, the constant $\mathrm{Mn_{Ga}}$ concentration of $5.4 \cdot 10^{15}$ cm^{-2} shown therein was assumed for all data presented in this section.

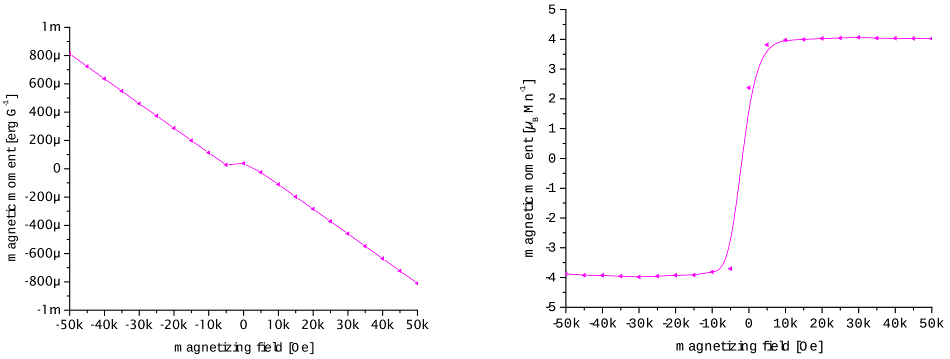

(a) Exemplary m vs. H data as recorded by the MPMS.

(b) Same data after subtraction of diamagnetic background and conversion to different units.

Fig. 3.2

The basic quantities accessible by these measurements are the saturation moment m_{sat} and, in the case of doing a more detailed complete loop, the coercivity and remnance. From m vs. T data, the Curie temperature T_C can be determined. It should be noted that this latter approach is much quicker, but also less accurate (usually yielding an error ±1 K), than application of the Arrott criterion [Arr57], as the cutoff has to be extrapolated from the steepest part of the slope prior to m being of the same magnitude as its statistical error. It also rests on knowledge about anisotropy, as it is only applicable for magnetic easy axes.

To check sample comparability - necessitated by the inherent laser fluctuations as mentioned in Section 2.2 - coarse data along one $\langle 110 \rangle$

direction was gathered for each sample. From the m vs. T series Figure 3.10 it becomes obvious that most samples are indeed the same within expected tolerances, with the two exceptions of #11 and #12. Considering all other samples, T_Cs are within an interval of < 3 K. The magnetic moments at lower T show more disparity, but are still clearly grouped. These differences arise partly from the random choice of either $[1\bar{1}0]$ or [110], one of which being a slightly harder axis as laid out in Section 2.1, and varying minor influences from the hard [001] axis due to imperfect in-plane alignment. Another factor is active sample area, which could for reasons related to the manufacturing process not be accurately determined in some cases.

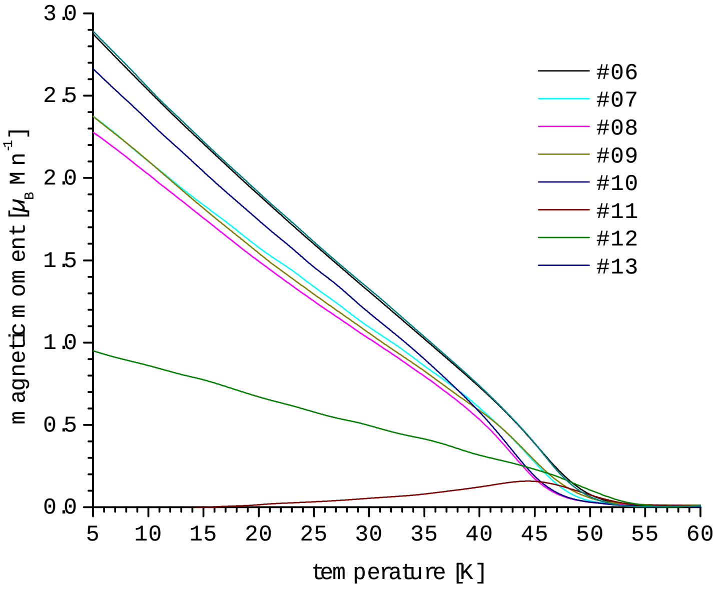

Fig. 3.3: m vs. T data for all samples.

Samples #11 and #12 show clearly distinct behavior. While the implausible low-T data with #11 arises from unintended field-cooling, both samples show lower slopes close to T_C (#12 over the whole range). Despite this, their respective T_Cs are remarkably similar to the other samples. This behavior is similar to what has been observed in GaMnAs samples irradiated at laser fluences slightly below the limit F_{XM} [Sca06], where some structural disorder remained between the different ranges of Mn implantation and melt front. It goes to show that crystal defects are only of secondary importance to robust magnetism in these materials. While impressive, for the study at hand a set of similar samples was required, and those two were thus precautionarily excluded.

The corresponding m vs. H data only has limited usefulness to establish comparability. All the samples exhibit nicely saturating magnetization, with an average $m_{sat} = 3.5 \pm 0.4\ \mu_{\mathrm{B}}\,\mathrm{Mn}_{\mathrm{Ga}}^{-1}$, thus well in agreement with previously established values [Sca05]. The spread in values here is due to the second reason cited above in the m vs. T case, but also due to the fact that diamagnetic background removal can be unreliable at high fields. At 5 T, the background is generally one order of magnitude larger than the actual signal, and thus measurement errors can be amplified and propagated to m_{sat}.

These results validate the approach of using one sample for SQUID magnetometry, another one for transport measurements.

Hysteresis loops were, due to time constraints, only gathered for uncompensated samples and for one after the last ion irradiation step. In the former case, the results are in line with those previously presented [Bih07], exhibiting a hard out-of-plane axis and two easy ones in-plane, with one of those being slightly harder and exhibiting the characteristic “kinked" loop. These loops in Figure 3.4 nicely showcase the certainly ferromagnetic properties of the GaMnP system. At the highest compensation level, the in-plane axes are hardly distinguishable any more. While already appearing paramagnetic at a first glance, especially the $[1\bar{1}0]$ alignment still shows coercivity of 0.5 Oe and remnance of 0.015 $\mu_\mathrm{B}\,\mathrm{Mn}_\mathrm{Ga}^{-1}$ (see Figure 3.5), both larger than the measurement errors.

After each ion implantation step, samples were measured along both [110] and $[1\bar{1}0]$ directions. Measurements along [001] were precluded by MPMS sample size constraints for that geometry. Thus the m vs. T data presents an interesting glimpse - the measurements are after all only at one magnetizing field - of the development of the anisotropy field. This evolution is showcased in Figure 3.6 and Figure 3.7. While hardly distinguishable for the as-manufactured samples, the axis show sharply distinct behavior already at very low levels of compensation. This indicates a fast transition from “kinked" to “wasp-waisted" hysteresis loops along $[1\bar{1}0]$, with an only slowly contracting “waist", as observed and modeled in [Sto08].

Extracting the Curie temperatures from the m vs. T data and plotting

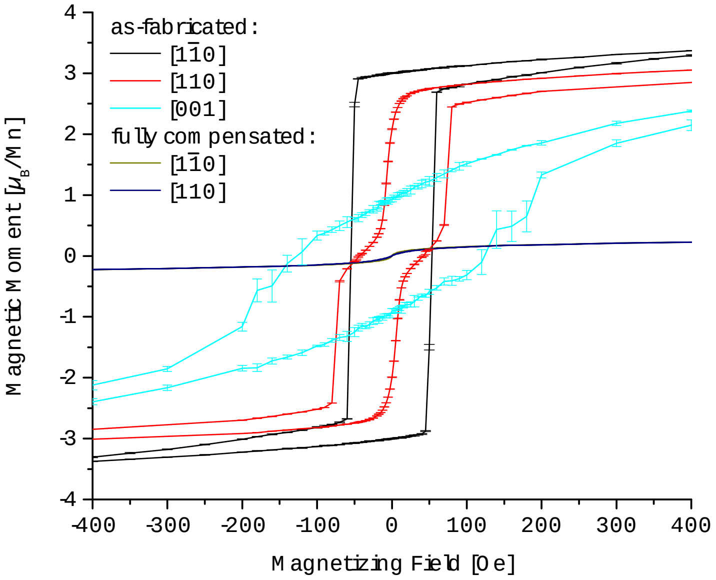

Fig. 3.4: Hysteresis loops measured for as-fabricated samples along [1$\bar{1}$0], [110] and [001] directions and for samples with $\Delta p = -6.5 \cdot 10^{15}$ cm^{-2} along [1$\bar{1}$0] and [110].

it over Δp yields part of Figure 3.8. There are currently various theoretical predictions for $T_C \propto p^\gamma$ ranging from the simple mean-field derived $\gamma = \frac{1}{3}$ [Jun05] to the $p - d$ Zener model prediction of $\gamma = 0.6 - 0.8$ [Nis10]. Theoretical work proposing a linear relationship as indicated here is not available, but it should be mentioned that such work has in general been far less extensive than that on $T_C \propto x$. On the whole, however, the models available are neither confirmed nor disproven by these results, as power laws close to $\gamma = 1$ are possible within the statistical errors over the range considered.

What is exceedingly exciting about this data is that, if plotted alongside

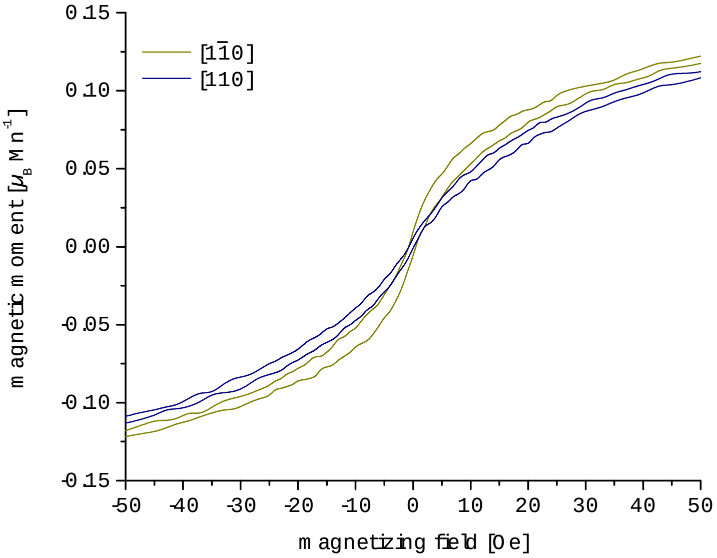

Fig. 3.5: Close-up of Hysteresis loops along [110] and [1$\bar{1}$0] for sample with $\Delta p = -6.5 \cdot 10^{15}$ cm^{-2}.

with similar data gathered from GaMnAs [May10] as is done in Figure 3.8, the trend is practically the same. This behavior is reminiscent of the behavior of T_C with Mn$_{\mathrm{Ga}}$ concentration, where the slopes in the region $x < 5$ % - considering strictly hole concentration, about the same regime as explored here - are also virtually the same for both materials [Sca06]. Relating to the power law behavior discussion above, it also bears mentioning that the nonlinear $T_C \propto x$ behavior in GaMnAs only becomes apparent for $x > 5$ % [Jun05].

The saturation moment - Figure 3.9 - also shows a decrease with Δp. To the first order, the relationship is again linear, although less obviously so. The effects of dominant diamagnetism at high fields as discussed above

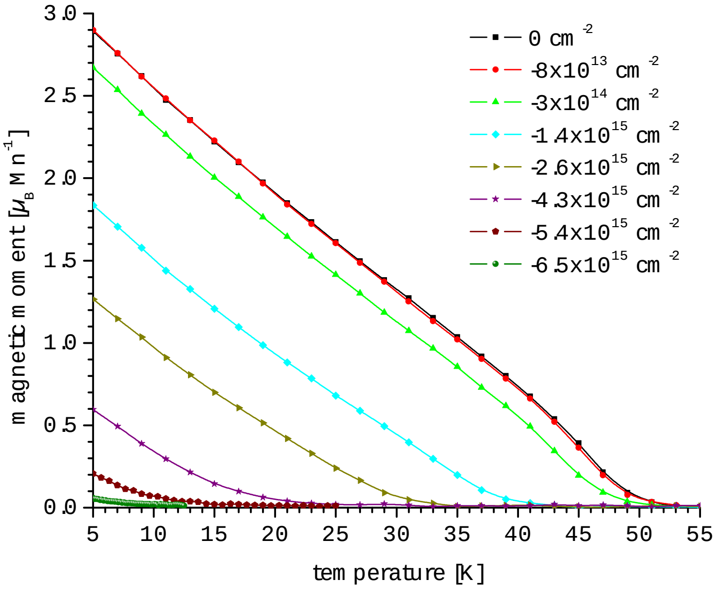

Fig. 3.6: m vs. T data along $[1\bar{1}0]$ direction for various Δp.

in a similar context are again a contributing factur, but it is believed to be mostly due to systematic errors. Especially obvious for $\Delta p \approx 3.1 \cdot 10^{15}$ cm^{-2} and $4.3 \cdot 10^{15}$ cm^{-2}, the m vs. H showed unusual behavior that can only be explained by SQUID nonlinearities, meaning that the actual field did not scale with the applied current - not entirely an uncommon problem in MPMSs [Ney08]. Minimal contamination with foreign, non-diamagnetic material can also never be excluded. It should be noted that both factors, especially the former, are not significant for m vs. T measurements due to the low fields utilized. The general behavior here, however, is in line with expectations, as Mn$_{\mathrm{Ga}}$ is being “inactivated", instead of being removed [May10].

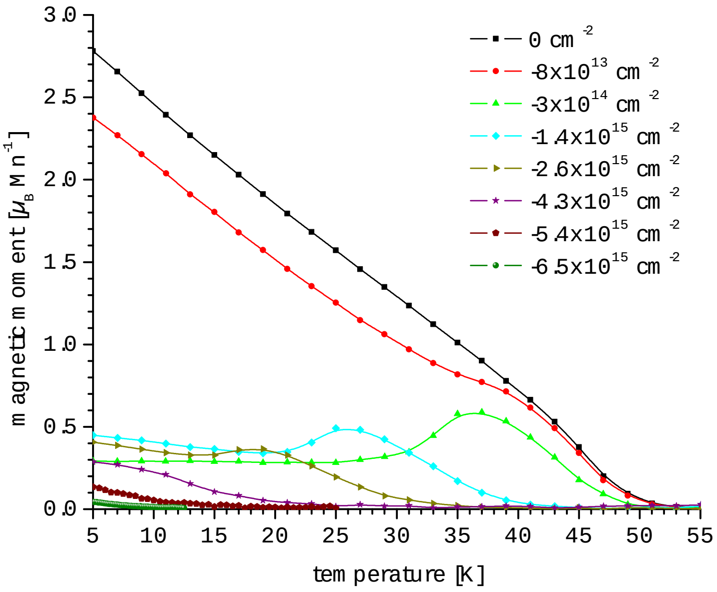

Fig. 3.7: m vs. T data along [110] direction for various Δp.

3.3 Electric Transport

The second focus of this project was electrical properties, which were investigated in the same liquid Helium cooled magnetotransport setup as was used for Hall effect measurements, although the magnet was not used for the measurements detailed here. Four pressed-on Indium contacts in Van der Pauw geometry were applied to the samples of interest, and sheet resistivity ρ_s was determined at different temperatures T, with data points roughly equally spaced in T^{-1}.

First, sample comparability was again checked, although here only with two samples. The results in Figure 3.10 strengthen what has been estab-

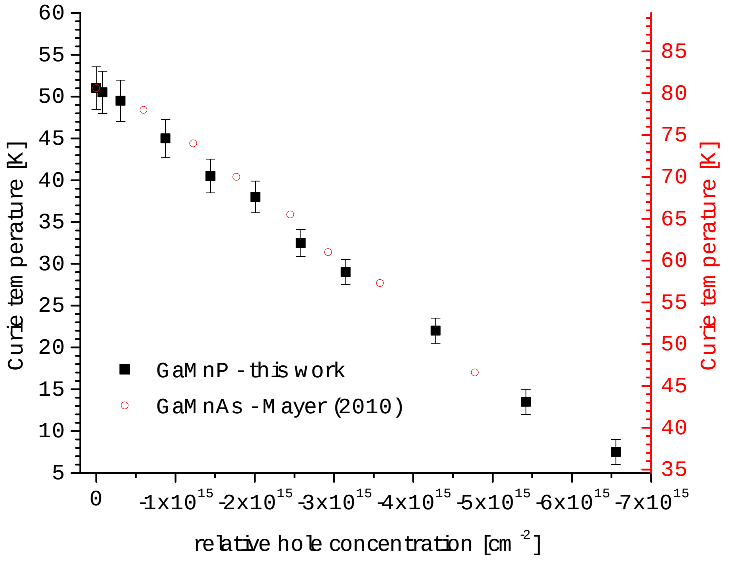

Fig. 3.8: Curie temperatures from this work on GaMnP for various levels of compensation (black, left scale) and from [May10] for GaMnAs (red, right scale (simple shift by +29.6 K)).

lished by magnetometry - the samples exhibit almost identical properties. The small deviation can be attributed to variations in contact quality, which is significantly smaller than that between different stages of hole compensation.

The plot also illustrates the problems encountered in these measurements. The main reason behind all the following are the highly insulating properties, well demonstrated here even for as-fabricated GaMnP. One of the issues were charging effects, which were most pronounced at very low temperatures and high resistivities, resulting in the measurement error being loosely proportional to those factors. While data was gathered up to $10^{11}\ \Omega\,\mathrm{cm}^{-1}$

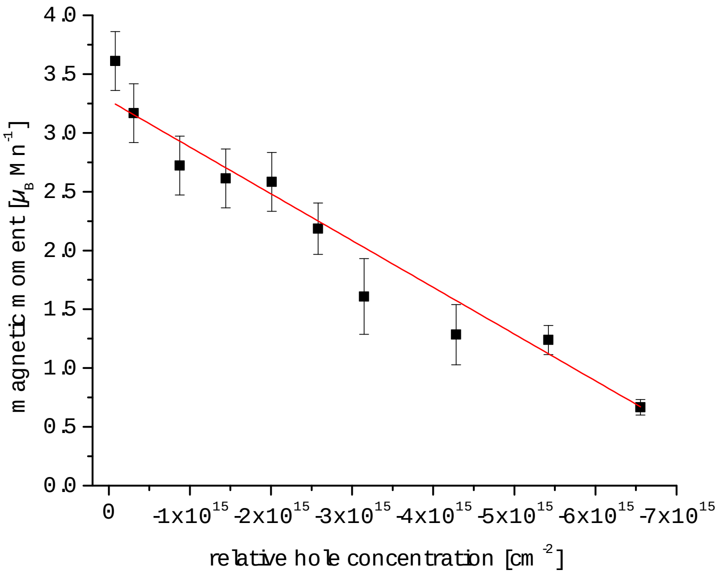

Fig. 3.9: Saturation moments for various Δp.

and down to 5 K, the error was deemed too great close to these limits of the experimental setup and analysis was restricted to the ranges depicted. Another issue were the Indium contacts, which in some cases caused non-Ohmic behavior, as evidenced by kinks in the resistivity data at those points where current was adapted to keep voltage within the bounds appropriate for the instruments. While, despite jumps in current generally of more than one order of magnitude, mostly only of minor impact on the resistivity as in the data from the Ar^+ implanted samples in the plot around 16 K, it proved significant in some measurements, which prompted a switch in samples for transport measurements from #10 to #09.

Resistivity measurements were performed after each step of ion irradia-

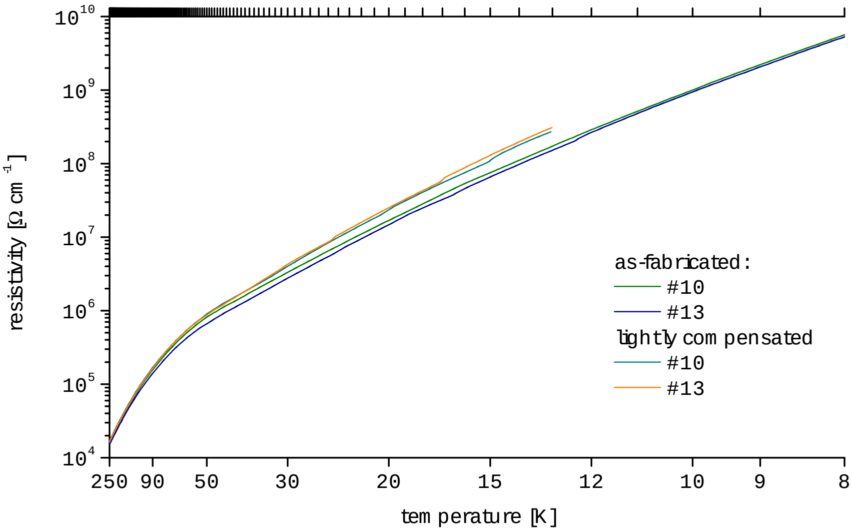

Fig. 3.10: Resistivity measurements on samples #10 and #13 as-fabricated and for $\Delta p = 8 \cdot 10^{13}$ cm^{-2}, plotted along a T^{-1} scale.

tion, and the composite results are displayed in Figure 3.11. The general trend of resistivity increasing with hole compensation is in line with expectations. At least for the lower half of the measurements, two distinct mechanisms seem to be involved in transport - conforming with theory as outlined in Section 2.1, while for the other half this is not immediately obvious. The transition between mechanisms seems to occur in the range of 60 K to 70 K, and not scale with T_C, as previously speculated [Sca05; Far06]. An impressive feature that bears mentioning is the resistivity for the fully compensated samples which can be extrapolated to be at least in the Petaohm-range at their T_Cs.

Fits with the simple model of $\rho = \left(\frac{1}{\rho_1} e^{-\frac{\varepsilon_1}{kT}} + \frac{1}{\rho_3} e^{-\frac{\varepsilon_3}{kT}}\right)^{-1}$ yield usable,

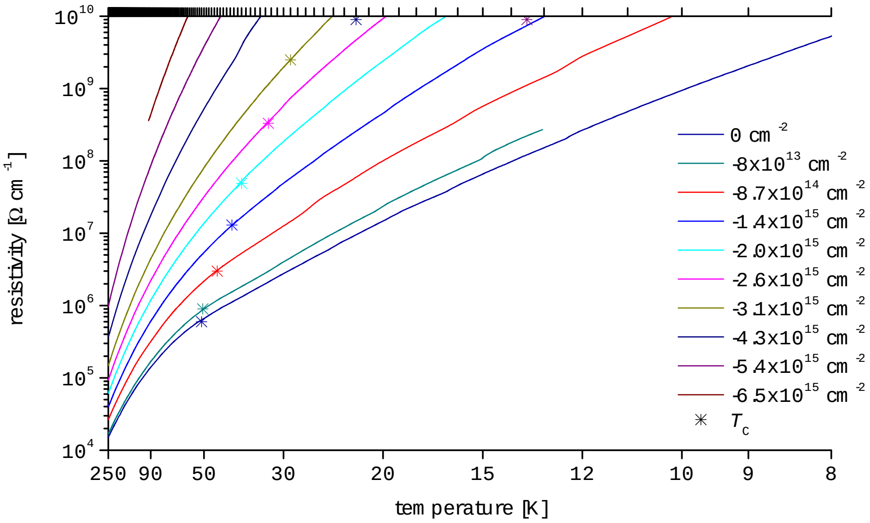

Fig. 3.11: Resistivity measurements for various Δp and respective T_Cs.

albeit due to its known shortcomings (see Section 2.1) imperfect, results, as shown in Figure 3.12. The starting values for the activation energies from Figure 3.13 are in good agreement with previously obtained ones, and the observed increase is in line with expectations. In the case of ε_1, it is caused by the shift in Fermi energy resulting from compensation [Sca05], while for ε_3 it is reasonable to assume an impediment of the hopping mechanism by the compensating defects.

3.4 Structural Analysis

To verify whether the effects observed were indeed due to compensation effects as intended or rather due to a reduction in the active Manganese,

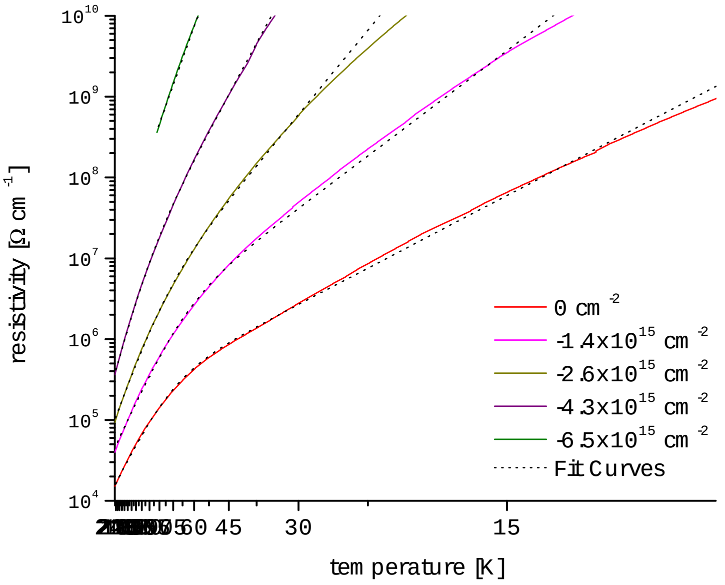

Fig. 3.12: Selected resistivity data and corresponding fits of model described in text.

the structure was investigated by way of chemically sensitive ion beam techniques. Specifically, samples before, at the final stage of and at an intermediate stage of Argon implantation were studied by Rutherford backscattering spectrometry (RBS) and particle induced X-ray emission (PIXE).

As these techniques are neither as intuitive nor as widely used as the others applied, some background information may be helpful. RBS and PIXE, which can be conducted in parallel, are based on the acceleration of ions - in this case $^4He^+$ at an energy of 2 MeV - onto the sample and analyzing backscattered ions and emitted X-rays, respectively.

The energy spectrum of the backscattered ions carries three kinds of

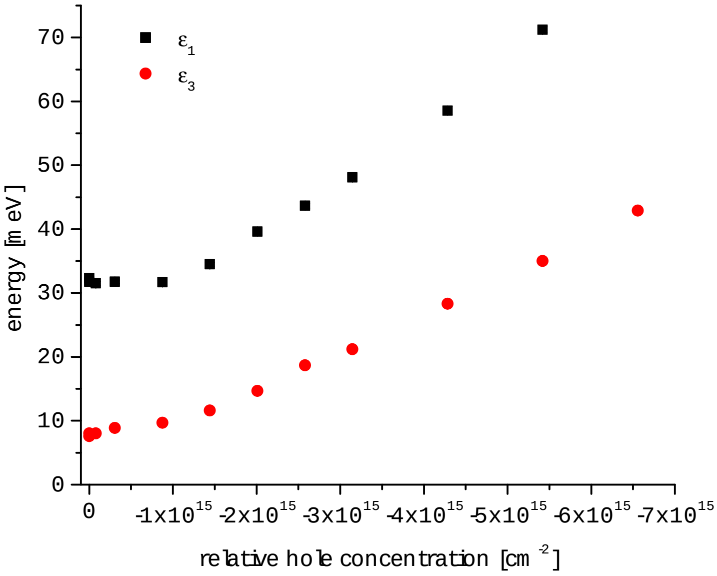

Fig. 3.13: Transport activation energies as determined by fitting.

information: chemical information on the scattering atom, information on their abundance, and information on their depth profile. The first can be derived through the so-called kinematic factor, which is the ratio of the ion energies before and after scattering on a surface atom. *Via* the laws of conservation of energy and momentum, it can be shown to depend - apart from the scattering angle - only on the masses of the involved particles, one of which is known. Quantitative information is accessible through the scattering cross-section, which again depends on scattering angle and atomic masses and is thus known, and which determines the scattering yield. Finally, information about the depth of the scattering event is available because the former two relations only hold for surface atom scattering. If an ion is backscattered on an embedded atom, it will lose energy on its path through the sample by inelastic interactions with the other sample atoms. The chances of dual backscattering are negligible, so the relevant contribution is interaction with the electron shells, exciting or ionizing the atoms. With some additional considerations, a linear correlation between the energy of a backscattered ions and the characteristic stopping cross-section of the material becomes apparent. Consequently, RBS spectra of non-trivial samples present themselves as an overlay of the depth profiles for each chemical species. This is ideal for samples where dopants are heavier than the matrix, but obfuscates matters when the dopant is lighter than even one of the matrix constituents - as is the case in GaMnP - because the signal of the dopant will be dominated by that of the much more abundant and heavier (thus also presenting a larger cross-section) element. [Chu73]

The energy spectrum of the emitted X-rays does not suffer from this caveat [Dav92]. When the high-energy ion excites or ionizes an atom, characteristic X-rays are emitted when the atom relaxes - especially K_α - and their energy conserved while traversing the sample. Their quantity depends somewhat on depth, because at some point the incident ion will have lost too much energy to excite an inner-shell electron. For the Mn-implanted region close to the surface, however, this can be neglected. Thus yield is a direct function of element abundance. By comparing the ratio of $\mathrm{Ga}-\mathrm{K}_\alpha$ to $\mathrm{Mn}-\mathrm{K}_\alpha$ with that of a reference sample, the absolute quantity of implanted Manganese can easily be determined.

The real strength of these ion beam techniques when applied to crystalline samples, however, is when channeling is utilized. By comparing spectra gathered at a “random" ion incidence angle (*i.e.* one not coinciding with any lattice vectors) to those gathered along major lattice axes, information on crystal structure - especially on defects - becomes accessible [Fel82]. Among the figures of interest is the fraction of substitutional Mn, which can be calculated as $f_{sub} \approx \frac{1-\chi_{min}^{impurity}}{1-\chi_{min}^{lattice}}$, where χ is the ratio of random to channeled yield. Specifically, $\chi_{min}^{impurity}$ is determined from the ratio of the integrated $\mathrm{Mn}-\mathrm{K}_{\alpha}$ peaks, and $\chi_{min}^{lattice}$ from the ratio of integrated RBS spectra in the range corresponding to the Ga signals from the GaMnP layer [Sca06].

In Table 3.1, the numeric results of these measurements are presented. The most important conclusion to be drawn from these is that the active Mn concentration is virtually the same (averaging $5.4 \cdot 10^{15}$ cm^{-2}), considering these measurements were conducted on three different samples. Thus, the effects observed in SQUID and transport measurements can be assumed to indeed be due to compensation, not compositional changes. Another apparent effect is that non-substitutional Manganese is removed with processing. It seems unlikely that bombardment with the small ion doses utilized would result in either sputtering or lattice integration. The most probable cause for this decrease is sample processing inbetween ion implantations. Specifically, the compensated samples used here were additionally treated for short periods with HCl to remove the Indium contacts that had been applied to them. This appears to have removed more of the damaged surface layer from II-PLM processing, some of which was still left intact in the uncompensated sample, and which as laid out in Section 2.2 contains a higher concentration of “random" Mn.

Δp [cm^{-2}]	Mn [cm^{-2}]	f_{sub}	Mn$_{\mathrm{Ga}}$[cm^{-2}]
0	$8.6 \cdot 10^{15}$	0.67	$5.75 \cdot 10^{15}$
$-8.7 \cdot 10^{14}$	$7.3 \cdot 10^{15}$	0.73	$5.3 \cdot 10^{15}$
$-6.5 \cdot 10^{15}$	$6.3 \cdot 10^{15}$	0.83	$5.2 \cdot 10^{15}$

Table 3.1: Numerical results of RBS and PIXE. Errors are on the orders of 10 %, 20 % and20 % for the result columns, respectively.

The errors on the measurements bear further discussion. For PIXE - and thus the total Mn content - they are solely statistical, albeit large due to the low yields. In RBS, however, the situation is more complex. For illustration, Figure 3.14 shows the actual normalized RBS data for the samples. One feature that immediately becomes apparent are the differences in the unchanneled spectra close to the surface. Deviations from a step-like form could be indicative of not entirely random directions. As the method for calculating $\chi_{min}^{lattice}$ utilizes just this region, a possible systematic error is introduced. The situation is not dissimilar for the channeled spectra, as their shapes are distinctly different, and the integrated yield over the same region may not hold the same information in all of them. The marked difference between compensated and uncompensated samples again is attributed to sample processing. A comparison of the compensated samples shows an increase in Gallium disorder not so much in magnitude but in range, in agreement with Ga being displaced. These difficulties, rather than the statistical variations, make for the large errors cited.

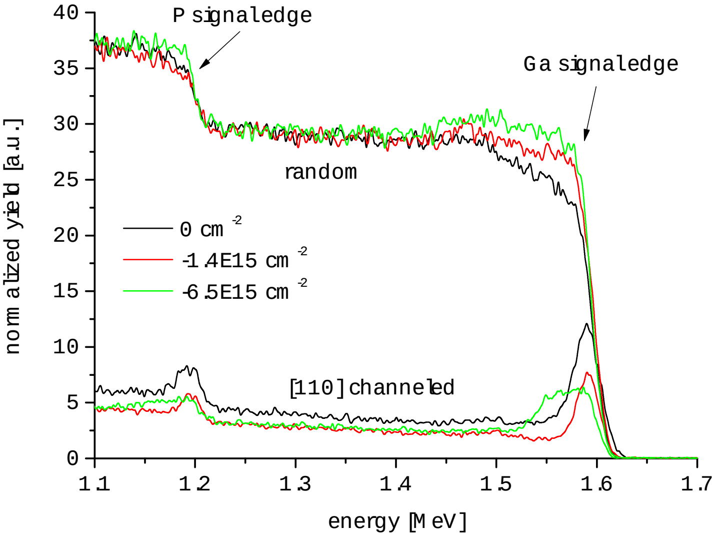

Fig. 3.14: Random and [110]-channeled RBS spectra for selected Δp.

4 Conclusions & Outlook

In this work, I have presented the control of the hole concentration in GaMnP over a very wide range. The resulting orders-of-magnitude changes in conductivity and the much more subtle changes in the magnetic response demonstrate the stability of ferromagnetic properties in this system, and enforce the notion that localized carriers are responsible for mediating the magnetic exchange. The most striking observation is the similarity in magnetic behavior between compensated GaMnP and GaMnAs. This is one more indicator that similar processes are involved in the two material systems despite the consiberably different electronic behavior, providing further evidence for the existence of a carrier-mediated phase on a continuum of carrier localization in III-Mn-V DMSs.

To fully appreciate the data gathered, more measurements and analysis are still forthcoming. The uncertain RBS/PIXE structural analysis is expected to be superseded by SIMS and TEM (transmission electron microscopy), which should establish beyond a reasonable doubt that the effects observed are solely due to compensation. Furthermore, a more complex transport model, likely to produce better fits and more accurate values for the activation energies, will be applied to the resistivity measurements, expected to produce better fits and more accurate values for the activation energies. These foreseen experimental and theoretical implementations, however, are not expected to significantly alter the interpretations presented.

Acknowledgments

Special thanks are due for my advisors, Alberta Bonanni at JKU and Oscar Dubon at UCB, for the fruitful discussions, their encouragement, and above all for supporting me in every way possible on my endeavor - before, during, and after.

I am also immensely grateful to Peter Stone, whose experience - which he shared so freely - was an invaluable resource.

To the whole Dubon group: thank you for accepting me as one of your own so readily, I really enjoyed working with you.

I want to thank Kin Man Yu for conducting the RBS/PIXE measurements and for subsequent illuminating discussions.

Last but not least, thanks go to the *Marshall Plan Foundation*, the *Macke Foundation* and the *Fonds zur Förderung der wissenschaftlichen Forschung* for their financial support.

Bibliography

[Arr57] A. Arrott. “Criterion for Ferromagnetism from Observations of Magnetic Isotherms”. In: *Phys. Rev.* 108 (1957), pp. 1394–1396.

[Bih07] C. Bihler et al. “Magnetocrystalline anisotropy and magnetization reversal in $\mathrm{Ga}_{1-x}\mathrm{Mn}_x\mathrm{P}$ synthesized by ion implantation and pulsed-laser melting”. In: *Phys. Rev. B* 75 (2007), p. 214419.

[Chu73] W. K. Chu et al. “Principles and applications of ion beam techniques for the analysis of solids and thin films”. In: *Thin Solid Films* 17 (1973), pp. 1–41.

[Cle85] B. Clerjaud. “Transition-metal impurities in III-V compounds”. In: *J. Phys. C* 18 (1985), pp. 3615–3661.

[Dav92] D. David. “New trends in ion-beam analysis”. In: *Surf. Sci. Rep.* 16 (1992), pp. 333–375.

[Die00] T. Dietl et al. “Zener Model Description of Ferromagnetism in Zinc-Blende Magnetic Semiconductors”. In: *Science* 287 (2000), pp. 1019–1022.

[Dub06] O. D. Dubon et al. “Doping and defect control of ferromagnetic semiconductors formed by ion implantation and pulsed-laser melting”. In: *Physica B* 376-377 (2006), pp. 630–634.

[Edm02] K. W. Edmonds et al. “Hall effect and hole densities in $Ga_{1-x}Mn_xAs$”. In: *Appl. Phys. Lett.* 81 (2002), pp. 3010–3012.

[Far06] R. Farshchi et al. “Compositional tuning of ferromagnetism in $Ga_{1-x}Mn_xP$”. In: *Solid State Commun.* 140 (2006), pp. 443–446.

[Fel82] L. Feldman et al. *Materials Analysis by Ion Channeling: Submicron Crystallography.* Academic Press, 1982.

[Jun05] T. Jungwirth et al. “Prospects for high temperature ferromagnetism in (Ga,Mn)As semiconductors”. In: *Phys. Rev. B* 72 (2005), p. 165204.

[Jun06] T. Jungwirth et al. “Theory of ferromagnetic (III,Mn)V semiconductors”. In: *Rev. Mod. Phys.* 78 (2006), pp. 809–864.

[Jun07] T. Jungwirth et al. “Character of states near the Fermi level in (Ga,Mn)As: Impurity to valence band crossover”. In: *Phys. Rev. B* 76 (2007), p. 125206.

[May10] M. A. Mayer et al. “Electronic structure of $Ga_{1-x}Mn_xAs$ analyzed according to hole-concentration-dependent measurements”. In: *Phys. Rev. B* 81 (2010), p. 045205.

[Ney08] A. Ney et al. “Limitations of measuring small magnetic signals of samples deposited on a diamagnetic substrate”. In: *J. Magn. Magn. Mater.* 320 (2008), pp. 3341–3346.

[Nis10] Y. Nishitani et al. “Curie temperature versus hole concentration in field-effect structures of $Ga_{1-x}Mn_xAs$”. In: *Phys. Rev. B* 81 (2010), p. 045208.

[Nov08] V. Novák et al. “Curie Point Singularity in the Temperature Derivative of Resistivity in (Ga,Mn)As”. In: *Phys. Rev. Lett.* 101 (2008), p. 077201.

[Ohn92] H. Ohno et al. “Magnetotransport properties of p-type (In,Mn)As diluted magnetic III-V semiconductors”. In: *Phys. Rev. Lett.* 68 (1992), pp. 2664–2667.

[Ove01] M. E. Overberg et al. “Magnetic properties of P-type GaMnP grown by molecular-beam epitaxy”. In: *Appl. Phys. Lett.* 79 (2001), pp. 3128–3130.

[Pea88] S. J. Pearton et al. “Ion implantation damage and annealing in InAs, GaSb, and GaP”. In: *J. Appl. Phys.* 64 (1988), pp. 629–636.

[Ruz04] D. Ruzmetov et al. “High-temperature Hall effect in $Ga_{1-x}Mn_xAs$”. In: *Phys. Rev. B* 69 (2004), p. 155207.

[Sca03] M. A. Scarpulla et al. "Diluted magnetic semiconductors formed by ion implantation and pulsed-laser melting". In: *Physica B* 340-342 (2003), pp. 908–912.

[Sca05] M. A. Scarpulla et al. "Ferromagnetism in $Ga_{1-x}Mn_xP$: Evidence for Inter-Mn Exchange Mediated by Localized Holes within a Detached Impurity Band". In: *Phys. Rev. Lett.* 95 (2005), p. 207204.

[Sca06] M. A. Scarpulla. "III-Mn-V Ferromagnetic Semiconductors Synthesized by Ion Implantation and Pulsed-Laser Melting". PhD thesis. University of California, Berkeley, 2006.

[Sca08a] M. A. Scarpulla et al. "Electrical transport and ferromagnetism in $Ga_{1-x}Mn_xAs$ synthesized by ion implantation and pulsed-laser melting". In: *J. Appl. Phys.* 103 (2008), p. 073913.

[Sca08b] M. A. Scarpulla et al. "Nonmagnetic compensation in ferromagnetic $Ga_{1-x}Mn_xAs$ and $Ga_{1-x}Mn_xP$ synthesized by ion implantation and pulsed-laser melting". In: *J. Appl. Phys.* 103 (2008), p. 123906.

[Shk84] B. I. Shklovskii et al. *Electronic Properties of Doped Semiconductors*. Springer-Verlag, 1984.

[Sik01] V. Siklitsky et al. *New Semiconductor Materials. Characteristics and Properties*. `http://www.ioffe.rssi.ru/SVA/NSM/`. 2001.

[Sto06] P. R. Stone et al. “Mn $L_{3,2}$ x-ray absorption and magnetic circular dichroism in ferromagnetic $Ga_{1-x}Mn_xP$”. In: *Appl. Phys. Lett.* 89 (2006), p. 012504.

[Sto07] P. R. Stone et al. “Tuning of ferromagnetism through anion substitution in Ga-Mn-pnictide ferromagnetic semiconductors”. In: *Physica B* 401-402 (2007), pp. 454–457.

[Sto08] P. R. Stone et al. “Compensation-dependent in-plane magnetization reversal processes in $Ga_{1-x}Mn_xP_{1-y}S_y$”. In: *Phys. Rev. B* 78 (2008), p. 214421.

[Wal88] W. Walukiewicz. “Mechanism of Fermi-level stabilization in semiconductors”. In: *Phys. Rev. B* 37 (1988), pp. 4760–4763.

[Wal89] W. Walukiewicz. “Amphoteric native defects in semiconductors”. In: *Appl. Phys. Lett.* 54 (1989), pp. 2094–2096.

[Yu02] K. M. Yu et al. “Determination of free hole concentration in ferromagnetic $Ga_{1-x}Mn_xAs$ using electrochemical capacitance-voltage profiling”. In: *Appl. Phys. Lett.* 81 (2002), pp. 844–846.

[Zie08] J. F. Ziegler et al. *SRIM 2008.04*. `http://www.srim.org/`. 2008.